# Investigation of Chlorinated Silicon Nanoparticles and In situ Analysis of the Size Distribution of Plasma Produced Particles

**A THESIS**
**SUBMITTED TO THE FACULTY OF THE GRADUATE SCHOOL**
**OF THE UNIVERSITY OF MINNESOTA**
**BY**

**Jasmine Nalani Johnson**

**IN PARTIAL FULFILLMENT OF THE REQUIREMENTS**
**FOR THE DEGREE OF**
**MASTER OF SCIENCE**

**Uwe Kortshagen, Advisor**

**October, 2017**

© Jasmine Nalani Johnson 2017
ALL RIGHTS RESERVED

# Acknowledgements

First and foremost, I want to thank my mother and grandmother for supporting me throughout my studies, and always being there when things got tough. I also want to thank my fellow lab mates for all their help and patience with my questions. I would like to acknowledge the MRSEC program and NSF for providing funding and the opportunity to collaborate with like-minded scientists. Some data included in this thesis were taken at the University of Minnesota's Characerization Facility.

## Abstract

Chlorine terminated silicon nanoparticles are produced from a non equilibrium plasma setup. The reactive chlorinated surface is exploited to functionalize the particles using Grignard chemistry and to stabilize the particles in solvent. By functionalizing the particles using Grignard chemistry, the particles form an optically clear solution in diethyl ether that is stable for four months. Chlorine surface coverage was successfully modulated by changing the precursor flowrate during synthesis. The solubility of as-produced particles in methyl ethyl ketone was found to be related to the amount of precursor used during synthesis.

A low pressure differential mobility analyzer (LPDMA) was installed downstream of a silicon nanocrystal plasma reactor in order to take *in situ* measurements of particle size distributions. Roughly equal amounts of positive and negative particles are observed. Size distributions of particles measured by the LPDMA are found to be much broader than those observed in TEM. This broadening is believed to be due to inflight coagulation. Inserting a mesh downstream of the plasma reduced the broadness of the distributions.

# Contents

# List of Tables

# List of Figures

# Chapter 1

# Plasma Synthesis of Chlorinated Silicon Nanoparticles

## 1.1 Introduction

The study of quantum dots is useful in a variety of applications including LED technology, solar applications and fluorescent dyes. Quantum dots are crystals that are small enough to have significantly different properties from the corresponding bulk material. The property this research is concerned with is photoluminescence (PL). When the radii of the crystals are comparable to their exciton Bohr radius, the energy states of their electrons are more similar to those of single atoms than the bulk material, and they must gain and lose energy in discrete amounts. This quantum confined state results in excited particles releasing energy in the form of photons instead of releasing heat or vibrating when they relax. The bandgap energy of these particles is a function of the particle dimensions, which means the wavelength of light released can be tuned by changing the size of the particles.

The most studied quantum dots are made from elements in the II-VI and III-V groups that often contain toxic metals such as Cd. Group IV semiconductors such as Si and Ge can also be used for the production of quantum dots and are much less toxic, but they have not been as thoroughly studied. This is because it is difficult to attain useful PL from these quantum dots. Group IV semiconductors have an indirect band gap which means that they require a change in electron momentum in order to lose

energy which reduces efficiency of recombination of electrons and holes which result in PL. [1]

The PL of quantum dots can be quantified by measuring their quantum yield, which is defined as the percentage of light emitted divided by light absorbed by the dots. Many studies have shown that passivating the particle's surface with bonds to organic chains through functionalization reactions is an effective method of increasing quantum yield in silicon nanoparticles. [2–4] Additionally, Anthony and Kortshagen have shown that the quantum yield of silicon nanoparticles is improved by increasing crystallinity, with purely amorphous samples only reaching quantum yields of 2%. [5]

There are several techniques used to produce quantum dots, the most common of which is colloidal synthesis. Advantages of using a radio frequency (RF) plasma as opposed to liquid phase synthesis include relatively narrow size distribution, the ability to decompose high melting point precursors near room temperature, and fewer post production steps because solvents are not used during synthesis. [6] Plasma synthesis also allows the production of halide terminated nanoparticles in one step by simply choosing a precursor such as silicon tetrachloride ($SiCl_4$). However, halide terminated quantum dots produced in nonthermal plasmas quickly oxidize in the atmosphere and gain surface bonds to oxygen. The Si = O and Si-O-Si bonds serve as electronic trap states that prevent the proper electron hole recombination that results in photoluminescence, which leads to lower quantum yields. [7] The same problem occurs in many solvents. This can be especially problematic for biomedical applications which frequently require the particles to be suspended in an aqueous solution. The particles must be functionalized to improve their chemical stability and quantum yield.

Chlorinated silicon particles open up a variety of potential functionalization reactions to change the properties of the particle, such as reactions with Grignard reagents, alkyl reagents, or Williamson ether reagents. [8] A Grignard reagent is an alkyl magnesium halide that is commonly used to add carbon chains to molecules. The reagent acts as a nucleophile which will attack electron poor carbon sites such carbonyl groups or alkyl halides. The Grignard reaction has long been used to create organosilanes, facilitating the production of silicone technology. [9, 10] There has been much investigation of the action of Grignard reagents on bulk silicon and aqueous silanes, but there has not been much research on applying this reaction to nanoscale silicon powders. [9–12]

This reaction allows relatively simple functionalization pathway that can improve the particles stability in nonpolar solvents and prevent degradation due to oxidation by forming a protective layer of carbon chains to the particle surface.

The purpose of this research is to reach high quantum yields and colloidal stability with chlorine terminated silicon nanocrystals. Hydrogen terminated silicon is relatively well studied, but the chlorine terminated particles should be easier to functionalize due to the reactivity of chlorine. The effects that a chlorine terminated structure have on functionalization techniques require more study.

## 1.2 Experimental Methods

The reactor setup used for nanoparticle synthesis is very similar to that described by Mangolini *et al.* [13]. A 1 in outer diameter alumina tube is evacuated to a pressure of several Torr using a rotary vacuum pump. Copper ring electrodes are fixed to the outside of the the tube with 1 cm of space between them. Bias is supplied to the electrodes using a 13.56 MHz power supply. An LC matching network is used between the power supply and the electrodes to maximize power input to the plasma by matching impedance. Hydrogen, argon and $SiCl_4$ are sent through the RF plasma. Typical reactor pressures are 1-3 Torr. The hydrogen serves as a source of radicals that can initiate the nucleation of silicon nanoparticles by forming silyl trichloride radicals. These silyl radicals can attack neutral silicon tetrachloride species which leads to particle growth. [14] An alumina tube is used instead of glass to prevent etching of the tube from the corrosive chlorinated precursor as well as chlorinated species produced during the reaction. The rotary pump and pump oil are also made to withstand corrosive environments. Downstream of the plasma, the flow is accelerated through a flat plate stainless steel orifice and the particles are collected on a substrate by impaction or caught on a mesh. Orifices used by previous students made of polyether ether ketone (PEEK) were also tested, but these were observed to clog more quickly than the steel over long deposition times. The pressure is monitored both above and below this orifice.

X-ray diffraction (XRD) measurements were taken on 0.5 cm x 1 cm films impacted onto glass for 2-3 minutes. The samples were scanned using a Bruker D8 Discover 2D

with a cobalt radiation source belonging to the University of Minnesota's Characterization Facility. Diameter of particles were estimated through Scherrer fitting using Jade 8.0 software.

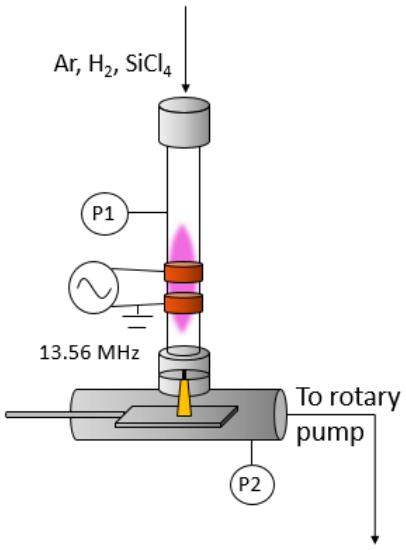


Figure 1.1: Plasma Reactor
A schematic of a flow through plasma reactor for gas phase synthesis of nanoparticles.

Relative chlorination of particle surface was estimated from comparing the peak area of Si-H to Si-Cl using FTIR data. The films were impacted onto aluminum coated silicon substrates and transported from the reactor to a nitrogen atmosphere glovebox. Diffuse reflectance spectra (DRIFT) and attenuated total reflectance (ATR) were taken using a Bruker Alpha-P spectrometer inside a nitrogen atmosphere glovebox. Peak areas were fitted using Origin 2016's peak fitting tool. Solvated or functionalized particles were scanned by dropcasting 0.5 mL onto Al-coated silicon and allowing the liquid to evaporate. Typical FTIR peak positions for chlorine terminated nanoparticles are listed in table 1.1.

Chlorine terminated particles were functionalized by adding approximately 5.0 mL of diethyl ether, 0.5 mL of dodecyl magnesium bromide and 5 mg of particles to a 7 ml glass vial inside the glovebox. Care was taken to transfer the particles between

Table 1.1: FTIR Peaks Observed in Chlorine Terminated Nanoparticles

| **Wavenumber ($cm^{-1}$)** | **Feature** |
|---|---|
| 2084, 626 | Si-$H_x$ |
| 1050 | Si-O-Si |
| 900 | $SiH_2$ (wag) |
| 850 | $SiH_3$ (scissor) |
| 780 | Si-Cl [15] |
| 740 | Si-Cl [15] |
| 550 | Si-Cl |

the reactor and the glovebox without exposure to air. Before bringing the solvent inside the glovebox, it was allowed to dry on 4Å molecular sieves for 1hr and the air in the headspace of the container was replaced with nitrogen using a Schlenk line for 10 seconds. Fully degassing diethyl ether using this method is difficult due to the high vapor pressure of the ether leading to much evaporation of the solvent. After adding the solution to the particles, the reaction proceeded immediately and was stirred on a stir plate for 1 hr.

Photoluminescence measurements were taken by adding 1.0 mL of the above mentioned solution to a 2 mL vial diluted to a concentration of about 1 mg/mL of particles. This was set in an integrating sphere with a 395 nm LED light source and an Ocean Optics HR4000 detector for UV-Vis. For NIR measurements, a white xenon lamp source with a narrow pass filter set to 400 nm and an InGaAs NIR detector were used.

For stability tests in methyl ethyl ketone (MEK), chlorine terminated silicon nanoparticles were impacted onto glass, and then weighed into a glass flask. Enough MEK was added to reach a concentration of 7 mg/mL. The samples were observed by eye immediately after being produced, and after 24 hours. The solvent was dried using 4Å sieves and degassed on a Schlenk line for 10 minutes before being added to the particles.

## 1.3 Controlling Particle Crystallinity

As reported elsewhere, the crystallinity of particles increases as the power supplied to the plasma increases. [14,16] For recipes including $SiCl_4$, much more power is necessary to achieve crystals compared to particles produced from silane. This can be seen from the sharpening of peaks of the nanocrystals's XRD spectrum as shown in figure 1.2. This

is likely due to a combination of factors including the energy absorption by exciting the vibrational modes of hydrogen and absorption of electrons by electronegative hydride ions once a bond is broken. [17] Previous work by Yasar-Inceoglu *et al.* also suggest chlorine incorporation into the nanocrystal requires more energy than hydrogen by bond strain on the Si-Si bonds in the crystal. [15]

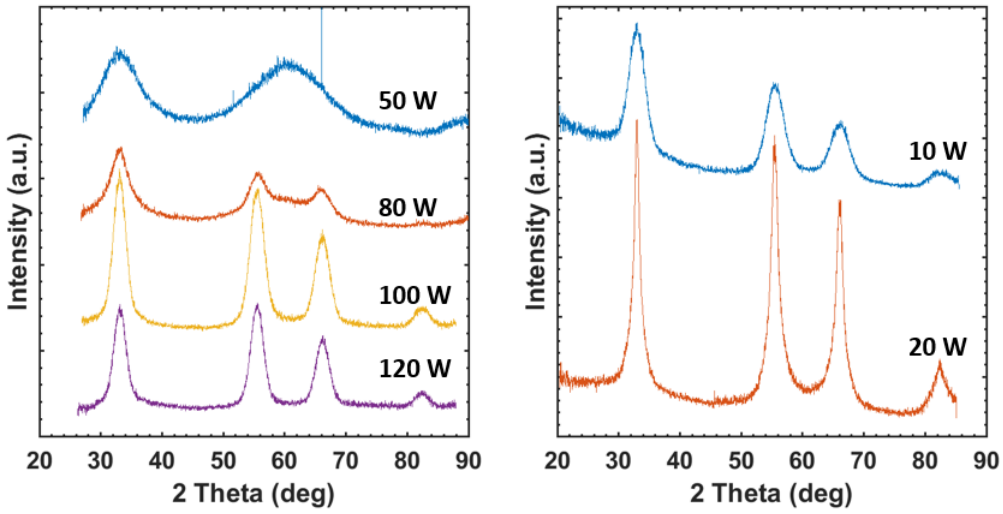


Figure 1.2: Particle Crystallinity
**Left:** XRD data of particles produced from $SiCl_4$ at several nominal input powers. Gas flowrates were 40 sccm Ar, 45 sccm $H_2$, and 2 sccm $SiCl_4$. Deposited for 3 minutes at a pressure of 2.1 Torr. **Right:** Particles produced from silane without hydrogen injection. Gas flowrates were 60 sccm Ar, and 14 sccm 5% $SiH_4$ in Ar. Deposited for 5 minutes at a pressure of 3.0 Torr.

## 1.4 Controlling Particle Size

Investigations by Gresback et al. [18] have shown that particle size scales with residence time. Residence time can be estimated according to the equation:

$$T_r = \frac{A_c * L_p}{Q * P}, \tag{1.1}$$

where $A_c$ is the cross sectional area of the tube, $L_p$ is the length of the plasma, $Q$ is the standardized total volumetric flow rate, and $P$ is the pressure in the reactor. To

the author's knowledge, the most thorough test of particle size control for particles produced using $SiCl_4$ were also performed by Gresback. [19] In an effort to produce particles smaller than 5 nm which would be sufficiently quantum confined for PL, several synthesis conditions were varied, including flowrates, tube diameter, and orifice slit width. Starting with a 2 cm outer diameter tube and a 0.5 mm slit orifice, flowrates were raised in order to decrease residence time.

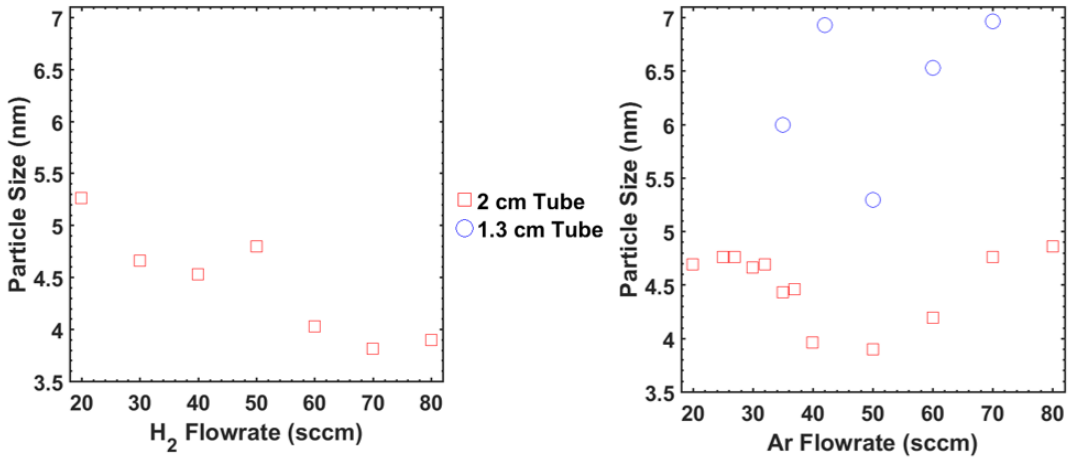


Figure 1.3: Particle Size as a Function of Carrier Flowrate
**Left:** Effect of changing $H_2$ flowrate with Ar held at 50 sccm. **Right:** Effect of changing Ar flowrate with $H_2$ held at 45 sccm. Size estimates from Scherrer fitting of XRD data.

However, because pressure and flowrate are coupled in the current reactor setup, the relationship between flowrate and residence time is nonlinear. This is especially obvious when increasing the Ar flow, as particle size starts to increase again after 60 sccm due to the increasing pressures. Plasma length is difficult to decrease because this parameter can also affect the crystallinity and deposition rate of the particles.

Two other tube sizes (1.2 cm and 1 cm inner diameter) were tested to see the effect of lowering the cross sectional area on particle size. No particles were collected on the substrate without decreasing the distance between the orifice and the substrate. This decreased distance combined with the smaller volume of the thinner tubes means that the same volumetric flowrates used in the thicker tube will lead to much higher impaction speeds. Because of the high impaction speeds, the deposits at these flowrates

form flaky films that adhere poorly on glass, aluminum coated silicon and carbon tape on glass. The only samples which formed films measurable in XRD were produced at lower flowrates than those produced in the 2 cm tube. At the lower flowrates tested, the thinner tubes actually produced larger particles.

Attempts were also made to use an orifice with a larger slit (0.75 mm), but no particles were collected. It is possible that attempts to decrease particle size drive the particles into the diffusive regime, which leads to difficulty collecting them through impaction. If this is the case, the collection problem could be alleviated by using a turbomolecular pump on the system to reduce collisions and reduce the effect of diffusion while collecting particles on a mesh.

Changing precursor flowrate had little effect on the particle size as shown in figure 1.4. Rather, increasing precursor flowrate appears to increase the ratio of silicon that forms an amorphous film on the reactor tube verses the amount that forms particles.

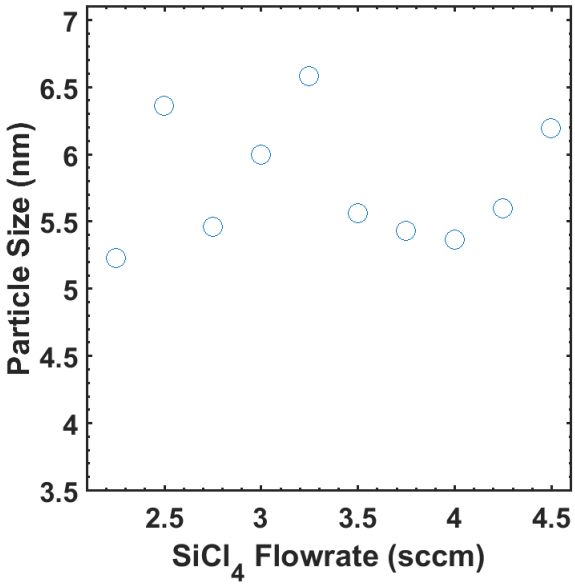


Figure 1.4: Particle Size as a Function of Precursor Flowarate
Shows the effect of changing $SiCl_4$ flowrate with 50 sccm Ar and 20 sccm $H_2$. Reactor pressure was 2.2 Torr.

## 1.5 Controlling Surface Chlorination

Silicon particles produced from $SiCl_4$ with hydrogen injection have surface bonds to both hydrogen and chlorine. The hydrogen that is used to initiate seeding can also attack the surface of the particles increasing the amount of hydrogen on the surface and creating HCl vapor. This means that the amount of chlorine on the surface can be increased by increasing the ratio of precursor to $H_2$. Increased chlorine termination is desirable because the particles' surface will be more reactive, which should lead to decreased reaction times and increased yield during passivating functionalization reactions. The ratio of chlorine to hydrogen termination should be related to the ratio of the peak areas of the silicon chloride peak and silicon hydride peak using FTIR. Due to complications involving the relationship of the peak intensity to the change in dipole strength of the excited bond, the ratio of peak area is not proportional to the relative concentration of bonds. An equal amount of Si-Cl bonds will show a larger peak than Si-H bonds, so without an internal standard to decouple the effects of the dipole from the concentration, FTIR alone cannot be used to find percentage of chlorine coverage on the particle surface. However, it can still be used qualitatively to determine change in chlorination between different samples.

Lowering the $H_2$ flowrate had little effect on the peak area ratio, but increasing the precursor flowrate causes an obvious increase in the ratio. Yasar-Inceoglu *et al.* also found little effect on surface chemistry through changing the amount of hydrogen dilution. [15] Although not shown in figure 1.5, precursor flowrates up to 5.5 sccm were tested. Further increase of the precursor flowrate past 4 sccm leads to excessive build up of amorphous silicon on the wall of the tube and in the orifice, and extremely low deposition rates, to the point it is difficult to collect enough film to scan the samples in FTIR before clogging of the orifice occurs.

Intuitively, one would expect that the important parameter for increasing surface chlorination should be the ratio of precursor to hydrogen feedrate, so it is unclear why changing the hydrogen flow does not seem to affect the surface chemistry of the particles, but an increase in precursor does. It is possible that even the lowest hydrogen flowrates tested provide enough H atoms to saturate the particle surface, while there is a general scarcity of Cl in the plasma.

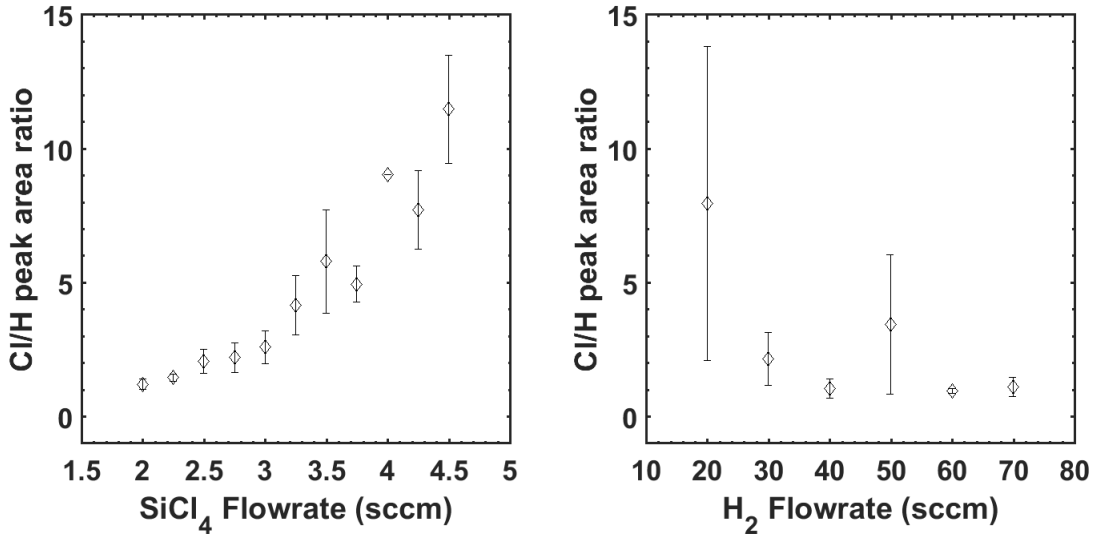


Figure 1.5: Cl/H Peak Area Ratio vs. Flowrate
**Right:** Particles produced with 20 sccm $H_2$ and 50 sccm Ar. Error bars represent one standard error from the mean value of three samples. **Left:** Particles produced with 2 sccm $SiCl_4$ and 50 sccm Ar

## 1.6 Grignard Functionalization

Since the particles are terminated with chlorine, functionalization methods such as the Grignard reaction are available. About 5 mg of particles are added to 5 mL of diethyl ether (DEE) and 0.5 mL dodecyl magnesium bromide. After adding the Grignard reagent to the particles in solution, they readily form an optically transparent suspension, and are stable for approximately four months. Before adding the reagent, the particles will not disperse in DEE even if agitated. Indefinite stability is possible by storing the solution in an air free environment. By visual inspection, there is no difference in the reaction for more highly chlorinated particles.

Unfortunately, drop casting solution containing the functionalized particles to perform FTIR only shows the signal from unreacted reagent, and does not show evidence of having changed the surface of the particles. In order to combat this problem, attempts were made to run the reaction without using an excess amount of the reagent. Lowering

the amount of reagent added to the particles yielded no reaction. In order to drive the reaction forward, the reactants were heated to 80°C and held at reflux on a Schlenk line. No reaction occurred after 48 hours.

It is well known that Grignard reagents break down in the presence of water or alcohols to produce a salt and an alkane (or alcohol in the case of water) according to reaction: $MgXR_1+R_2OH \rightarrow MgXOR_2+R_1H$. Attempts were made to decompose the remaining reagent by adding a very small amount of methanol, forming a salt precipitate and an alkane which can be evaporated away. However, the alcohol also affects the stability of the particles in solution. Also, the precipitate settles to the bottom after several hours, but re-suspends easily if the solution is in any way perturbed. It is possible to separate the liquid and solid phases more completely through centrifuging, but this process significantly decreases concentration of particles in solution as observed by color. After this separation, the spectra still look like the Grignard reagent even after an hour of drying. Results are summarized in figure 1.6.

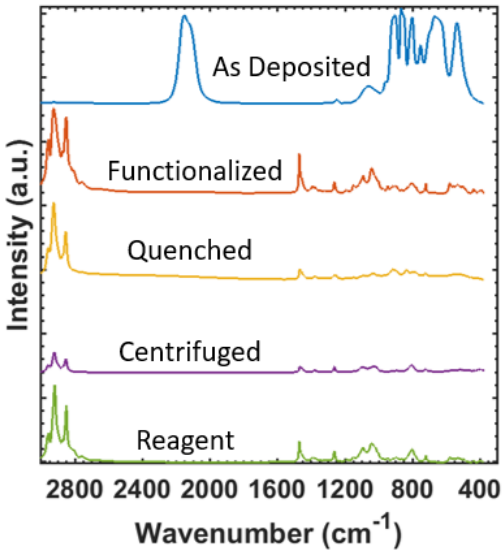


Figure 1.6: FTIR Comparison of Particles and Reagent
As deposited particles were scanned using DRIFT. Functionalized particles and Grignard reagent were scanned by dropcasting films for DRIFT analysis. Quenched and centrifuged particles were scanned using ATR due to low signal in DRIFT.

## 1.7 In Situ Oxidation

During the course of this research, there was sudden increase in the amount of oxidation on as produced particles as shown by the increase in intensity of the Si-O-Si peak in figure 1.7. The highly oxidized particles do not functionalize well with Grignard reagent, the reaction takes several minutes to complete, and they form a cloudy solution. This was originally believed to be due to air leaking into the reactor, but after decreasing the leak rate down to 4 mTorr/min by replacing old o-rings in the reactor, ensuring air free transport between the reactor and the FTIR setup, and increasing purge time before deposition, there were no observed changes in oxidation. Replacing the precursor with fresh $SiCl_4$ also had no effect. Wheeler had a similar problem and was able to solve this by using alumina tubes instead of glass. [16] The alumina was believed to be more resistant to etching by chlorine species generated during plasma synthesis than glass. In the current case, alumina tubes were used before and after the oxidation problem appeared. Also unlike the oxidation observed by Wheeler, no Si-OH peak is observed at 3350 $cm^{-1}$.

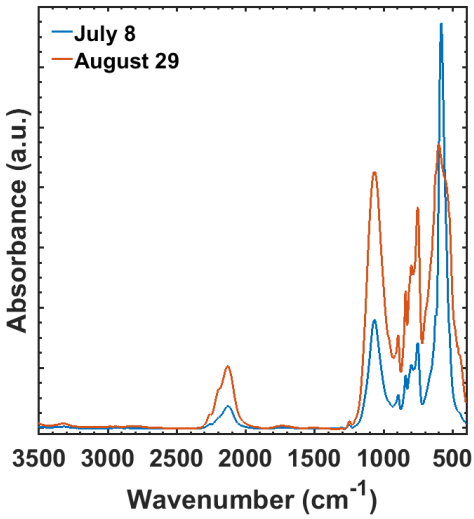


Figure 1.7: Oxidation of Particles
Si-O-Si vibration appears as a broad peak at 1050 $cm^{-1}$. Generally, as the particles are allowed to oxidize in air, the magnitude of this peak increases, and the magnitude of the Si-Cl peak at 550 $cm^{-1}$ decreases. Particles produced with 3 sccm $SiCl_4$, 20 sccm $H_2$ and 50 sccm Ar.

This problem was eventually alleviated by increasing hydrogen flowrate as shown in figure 1.8. Particles produced with this higher hydrogen flowrate react with Grignard reagent immediately to form an optically transparent solution. As discussed in section 1.5, there is little change in the amount of particle surface chlorination with a change in hydrogen flowrate, so this is not an especially detrimental solution. The cause of the oxidation remains unclear, but given that the same problem is not observed with silane produced particles in the same reactor, it seems to be related to chlorine species. Perhaps the reason the oxidation decreases with increased hydrogen flowrate is because the hydrogen is able to scavenge reactive chlorine species preventing them from causing oxidation.

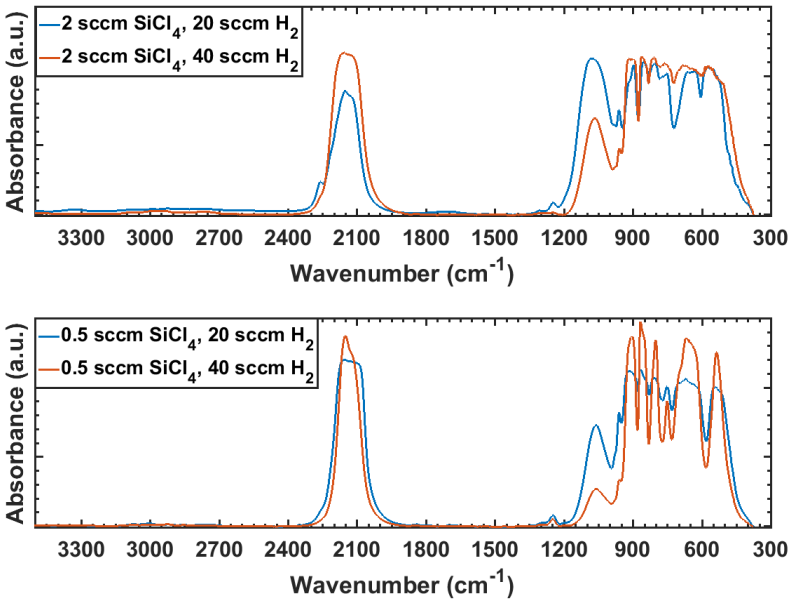


Figure 1.8: Effect of Increasing Hydrogen Flowrate
Regardless of precursor flowrate, increased hydrogen flow decreases the magnitude of the Si-O-Si peak at 1050 $cm^{-1}$. Total $H_2$ and Ar flowrate was held at 70 sccm.

## 1.8 Photoluminescence

Previous studies have found red luminescence from oxidized particles produced using $SiCl_4$. [16, 20] None of the process conditions reported here have shown emission even after being allowed to oxidize in air for several weeks. This includes particles deposited as films, powders, and particles that are reacted with Grignard reagent without being allowed to oxidize. Quantum yield measurements taken using an integrating sphere show that the particles absorb a large percentage of light, but do not emit. Scans were taken between 600 and 1200 nm. It is possible that this lack of PL is due to the relatively large diameter of the particles not producing the quantum confinement effect, although those studied by Wheeler were of similar and larger diameters. It is also possible that the same contamination of the particles that causes *in situ* oxidation are causing surface traps that do not permit emission of red light. However, literature suggests that even if smaller, cleaner particles are successfully produced, it may be difficult to observe PL from chlorine terminated silicon. Models show that chlorine incorporation leads to a significant red shifting of the band gap in silicon nanocrystals. [21,22] It is possible that remaining silicon chloride bonds after oxidation in air or Grignard functionalization are red shifting any emission from the particles past where it can be reliably observed using the detectors available to the author. It has also been suggested in literature that some complications may arise from halide exchange during the Grignard reaction. [23]

## 1.9 Solvating in Methyl Ethyl Ketone

Wheeler *et al.* found that chlorine terminated silicon nanopaticles are soluble in ketones and nitriles without being functionalized. [24] This is in contrast to undoped hydrogen terminated silicon particles which have only limited solubility in 1,2-dichlorobenzene and do not form optically transparent solutions without being functionalized. [24, 25] The current study is of how the solubility of these particles changes in response to increasing chlorination of the particles. According to the theory put forth by Wheeler in the previously mentioned work, there are hypervalent interactions between the electropositve silicon centers of atoms containing bonds to chlorine and the electronegative group in the solvent. This would imply that a more highly chlorinated surface leads to improved stability in such solvents.

Increased chlorination of the particle surface leads to visibly increased maximum concentration in methyl ethyl ketone, as well as duration of stability as shown in figure 1.9.

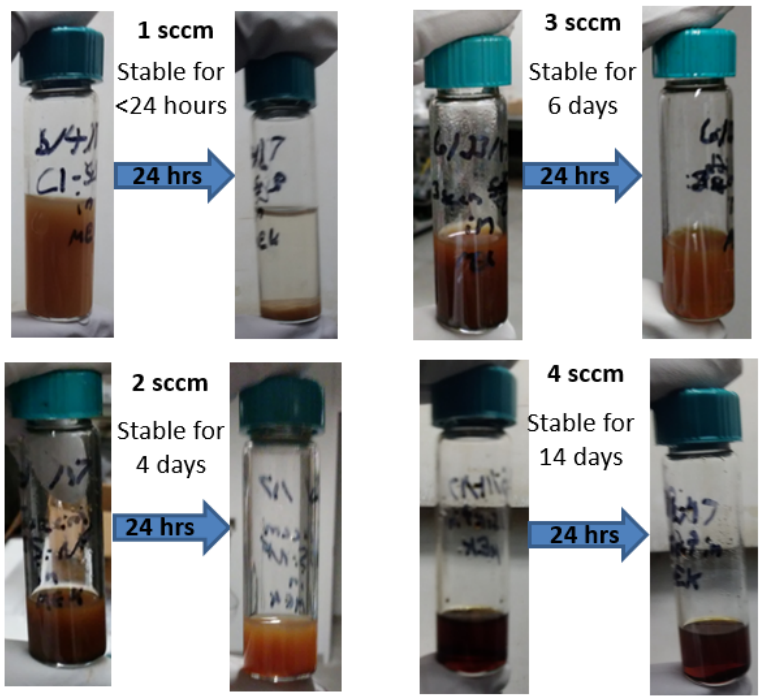


Figure 1.9: Stability of Particles in MEK
Images of as produced particles added to MEK on the right, images of the same samples allowed to sit overnight in an air free environment on the left. The amount of time the particles stay in solution without precipitating out is listed below the sample name. All samples have similar concentrations of 7 mg/mL. Only the 4 sccm $SiCl_4$ sample remains optically transparent after 24 hours. Particles produced with 30 sccm Ar and 40 sccm $H_2$ at 2.0 Torr

If this stability is due to hypervalent interactions as suggested by Wheeler et al., it is not surprising that increasing the number of bonds to chlorine will improve stability. With more bonds to chlorine on the surface, more of the surface silicon atoms will be in an electron poor state, which should facilitate the hypervalent interactions.

## 1.10 Conclusion

Partially chlorine terminated silicon nanocrystals were produced in a plasma. Particles were found to be between 4 and 7 nm in diameter depending on process conditions such as gas feed rates, tube size and reactor pressure. By functionalizing the particles using Grignard chemistry, the particles form an optically clear solution in diethyl ether that has a four month shelf life if kept in an air-tight vial, and is stable indefinitely if stored in an air-free environment. Chlorine surface coverage was successfully modulated by changing the precursor flowrate during synthesis, as determined qualitatively using FTIR data. The solubility of as-produced particles in methyl ethyl ketone was found to be related to the amount of precursor used during synthesis, and this is believed to be due to increased chlorine coverage on the surface of the particles leading to increased stability due to hypervalent interactions. The particles were not found to exhibit PL either as oxidized films or functionalized in solution between 600 and 1200 nm under any of the tested conditions.

## 1.11 Future Work

There is much work to be done in improving the synthesis of these particles. Especially important, further work must be undertaken to control oxidation of the particles during synthesis. This will allow a wider range of surface chlorination for further chemistry. As for the photoluminescent properties of chlorinated particles, more research is necessary to determine why they are so much less likely to luminesce than hydrogen terminated particles of a similar size. There may be other methods of making the particles smaller as well. In the current work there seemed to be a limit where it was unclear if the deposition rate was extremely low or if was simply no longer possible to collect the particles by impaction. Using a mesh for collection instead would clarify this.

It is interesting how the feed gas flowrates affect the surface chemistry of the particles. Using X-ray photoelectron spectroscopy or Rutherford backscattering instead of FTIR to get quantitative data on the chlorination percentage of the particles would help further studies into the sensitivity of the surface chemistry to process conditions. With more information on the products, it may be possible to fit the feedrates to a rate law to understand why increasing precursor has more effect on chlorination than

decreasing hydrogen dilution. These techniques were unfortunately unavailable in the current work due to lack of an air free transfer method. More quantitative measures would also be informative to understand the effects that chlorination has on stability in solution. For example, dynamic light scattering (DLS) could be used to quantify the concentration of particles in solution and to monitor how this concentration changes over time. Chlorination should allow several other functionalization reactions that were not studied here, such as Williamson ether synthesis or amino-dehalogenation.

# Chapter 2

# In situ Size Distribution Measurments using an LPDMA

## 2.1 Introduction

A correlation has been shown between spectral broadening of PL in silicon nanoparticles and size polydispersity. For this reason, many applications of silicon nanoparticles, such as biotracers or solar cells, can benefit from higher control of particle size distribution. [26, 27] Therefore, placing a low pressure differential mobility analyzer (LPDMA) downstream of the synthesis plasma is an attractive idea. DMAs separate aerosol populations according to their electrical mobility. This could be used for *in situ* feedback on particle size distribution as a plasma is running in order to test how the distribution changes in response to plasma conditions. There is also the possibility of collecting highly monodisperse particles after the LPDMA's selection stage.

To the author's knowledge, there have been relatively few previously published attempts to interface a plasma with a LPDMA. Nienow and Roberts connected a nonthermal RF plasma reactor to a set of two DMA's by pumping up to atmospheric pressure after the outlet of the plasma. They found expected trends in size distribution based on process conditions, but were unable to verify their distributions with TEM data. [28] Seol *et al.* successfully sent the outlet of a processing plasma into an LPDMA, but found a 14-50% discrepancy in mean diameter between their TEM data and the scans they got from the LPDMA. [29]

One of the major challenges of this work is the fact that the same low pressures that allow for plasma processing of material mean the gas is in a region near the minimum of its breakdown voltage. [17] This means that raising the voltage on the DMA electrode can easily create a discharge resulting in inability to take readings from the electrometer and damage to the electrode. Low pressures also lead to Brownian diffusion, which causes particles which are not of the selected mobility to exit with the monodisperse flow, reducing the signal to noise ratio from the DMA. [30] For these reasons, most DMA run at atmospheric pressure, and require modification in order to run at subatomic pressures. The following experiments were performed using an LPDMA that can run as low as 4 Torr, which is low enough to produce silicon crystals. Most silane plasma reactions in the Kortshagen lab are run between 1-3 Torr, so the process conditions cannot be directly compared to previous studies. Specifically, the increase in pressure dramatically increases the residence time in the plasma, resulting in larger particles. Much of the work in this section deals with attempts to increase the accuracy of the measurements taken from the LPDMA for use in characterizing plasma produced nanoparticles.

## 2.2 Experimental Methods

The LPDMA used in the following research belongs to the Hogan group, also at the University of Minnesota, and the research was conducted collaboratively with Xiaoshuang Chen from that group. A schematic of the setup and a table typical conditions are included in table 2.1 and figure 2.1.

Scans from the DMA were converted from voltages into concentration vs. size using the flowing relations:

$$Z_{pc} = \frac{Q_{sh} ln(\frac{R_2}{R_1})}{2\pi LV}, \tag{2.1}$$

where $Q_{sh}$ is the volumetric sheath flowrate, $Z_{pc}$ is the electrical mobility, $R_1$ and $R_2$ are the outer and inner diameter of the DMA's inner chamber, L is the length of the column, and V is the voltage drop across the plates. $Z_{pc}$ can then be inserted into 2.2 to find the diameter of the particle [31],

$$Z_{pc} = \frac{qeC_c}{3\pi\mu d_p}, \tag{2.2}$$

where $\mu$ is the viscosity, $q$ is the number of charges on the particle, $e$ is the charge on an electron, $C_c$ is Cunningham's correction factor, and $d_p$ is the particle diameter. [32] The concentration is determined by:

$$I = nqQ, \tag{2.3}$$

where $I$ is the current measured by the DMA's electrometer (converted from voltage), $n$ is the concentration of particles, $q$ is the number of charges on the particles, and $Q$ is the flowrate in the electrometer chamber after the nozzle. The flowrate after the nozzle in the DMA varies linearly with the pressure at P2 shown in figure 2.1. A calibration curve developed by Xiaoshuang Chen was used to find this flowrate.

Stainless steel mesh with various pore sizes were inserted in the centering ring for the KF fitting downstream of the reactor tube. Most of the scans reported here were taken using a 400 or 100 size mesh. A custom centering ring 3D printed from PLA (polyactic acid) was used to hold the mesh in place and isolate the mesh from the surrounding metal.

TEM images were taken using a Tecnai T12 microscope. The samples were collected by diffusion on copper grids on a pushrod downstream of the plasma but before entering the DMA.

Table 2.1: Typical Process Conditions for Plasma - LPDMA Experiments

| | |
|---|---|
| Total Aerosol Flowrate (sccm) | 64 |
| Silane Flowrate (sccm) | 1 - 7 |
| Argon Flowrate (sccm) | 63 - 57 |
| Sheath Flowrate (sccm $N_2$) | 910 |
| P1 (Torr) | 4.4 - 5.7 |
| P2 (Torr) | 0.47 - 0.57 |

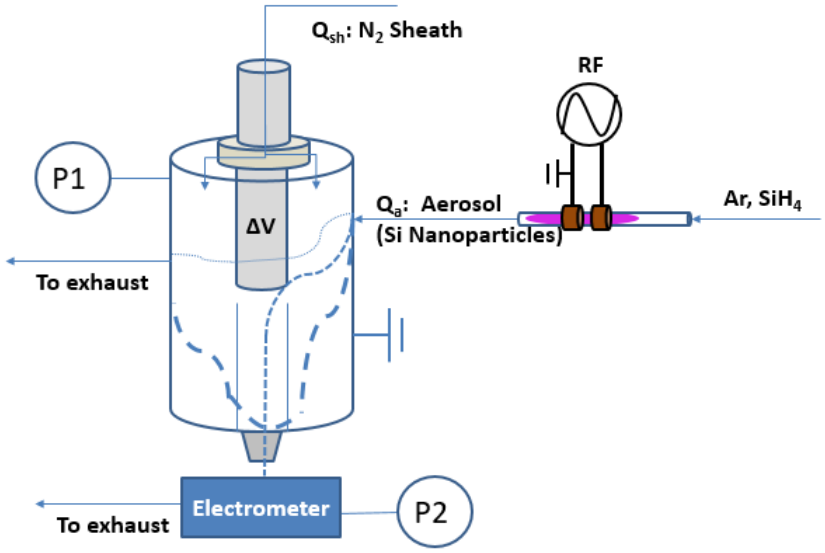


Figure 2.1: LPDMA with Plasma as Aerosol Feed
Schematic of the plasma - DMA system. Nanoparticles produced in the plasma serve as aerosol feed for the DMA. Changing the voltage drop between to the DMA's electrode and the inner wall of the surrounding chamber allows size selection of particles by their electromobility. Particles of the selected electromobility are able to pass into the second chamber and are accelerated through a nozzle toward the electrometer. Particles of other mobilities exit through the top chamber. Pressure is measured separately above and below the nozzle.

## 2.3 Deposition Rate

A mesh was inserted after the DMAs nozzle to test the possibility of collecting particles after they are size selected by the DMA. For this test, the DMA was set to hold a constant potential at the voltage that gave the greatest amount of signal for 5 sccm of $SiH_4$ during the scan test. 5 sccm was the highest flowrate that could be held several minutes without clogging leading to dramatic pressure increase (up to 1 Torr in 15 minutes) in the top chamber. However, no particles appeared to be collected after 30 minutes. Using the results from initial scans to estimate an expected deposition rate after the nozzle, it was found that it would take several years to collect the 5 mg required

to run a functionalization reaction using the particles. Due to the charge distribution discussed in section 2.4, only a fraction of the particles remain charged and are able to be selected by the DMA's electrode. Also, coagulation in the path between the reactor and the DMA causes a large number of particles to be outside of the range of the DMA. If these issues are addressed, it should increase the deposition rate, but it appears that using the current setup, collecting particles after the DMA is not viable.

## 2.4 Particle Charge Distribution

One of the first surprising points from scanning the output of the plasma with the DMA is that there are roughly equal numbers of positively and negatively charged particles, as shown in figure 2.2. Although most sources report that the particles in the plasma should be largely negatively charged due the mobility of electrons compared to positive ions in a nonequilibrium plasma as predicted by OML theory [33, 34], the results from the DMA imply that the particles reach a normal charge distribution around zero by the time the particles reach the sensor. Argarwal and Girshik modeled that for low residence times in the plasma there should be a non-negligible amount of positive particles, but in all cases they still found a bias toward negative particles. [35] This may be due to the electropositive sheath at the outlet of the plasma acting as a charge neutralizer for the particles.

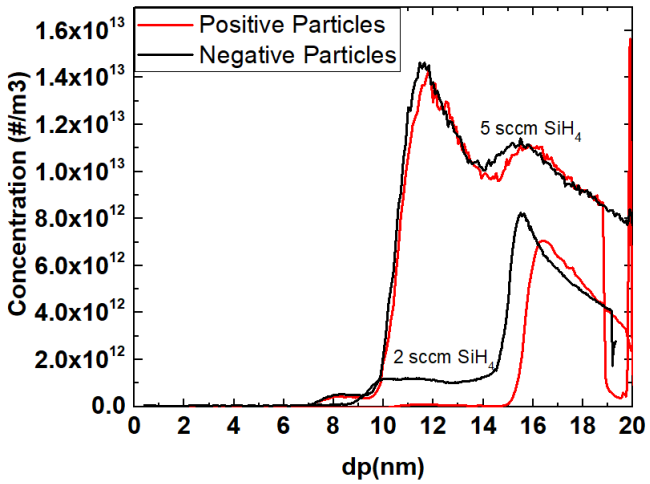


Figure 2.2: Concentration of Positive and Negative Particles
Scans taken by biasing the DMA electrode positively or negatively.

## 2.5 Coagulation

The nanoparticles generated in the aerosol line were characterized by XRD and TEM to sizes of 6 nm and 3.3 nm respectively. The discrepancy in these sizes is presumed to be related to the difference in collection method between the two samples. The XRD measurements were taken of particles that collected on a mesh downstream of the plasma, while the TEM samples were made by allowing the particles to collect on the grids by diffusion. Very small particles would be more likely to slip through the holes in the mesh (which are 40 $\mu$m wide) causing the mesh to act as a filter for the larger particles. A TEM image of the particles is included in figure 2.3.

As shown in figure 2.2, the particle sizes measured by the DMA far exceed the sizes of those found using XRD or TEM. This is believed to be due to in flight coagulation between the outlet of the plasma reactor and the DMA's sensor. The expected coagulation time of the particles can be estimated using a nondimensionalized and simplified version of the Smoluchowski coagulation equation:

$$\frac{dn^*}{d\tau} = t_r \frac{1}{2} k n_o n^{*2} \tag{2.4}$$

where $n^*$ is the nondimensionalized concentration, $\tau$ is the nondimensionalized time, $t_r$ is the characteristic coagulation time, $n_o$ is the particle concentration at $\tau = 0$, and the

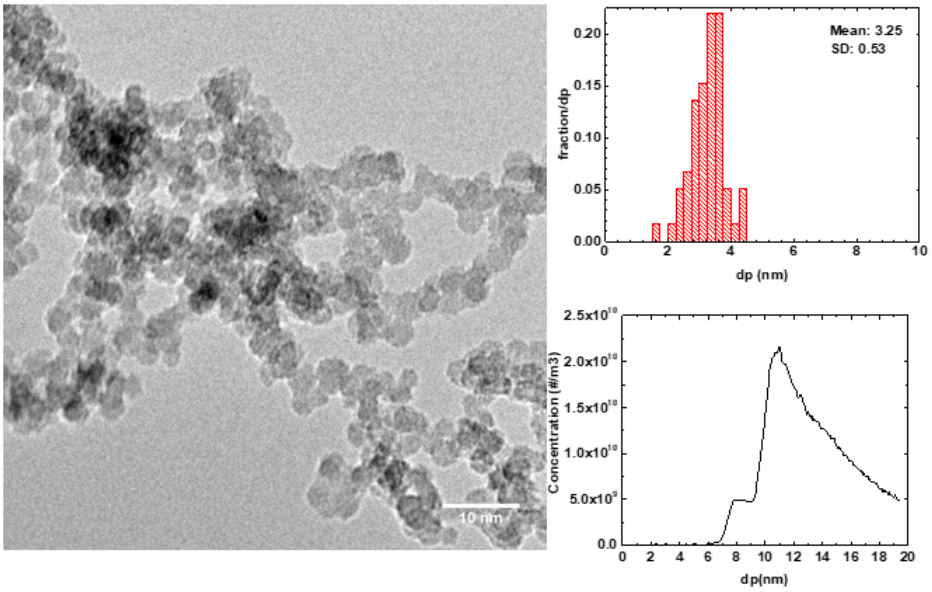


Figure 2.3: TEM of Particles Collected Between Reactor and DMA
**Left:** TEM image of particles taken by Katherine Hunter. **Upper Right:** Size distribution from TEM of 60 particles. **Lower Right:** Corresponding DMA scan taken during TEM sample collection.

collision kernel $k$ is:

$$k = (a_i + a_j)^2 \sqrt{\frac{8k_B T}{\pi m_{ij}}} \tag{2.5}$$

for ballistic coagulation. Where $a_i$ and $a_j$ are the radii of the colliding particles, $k_B$ is Boltzmann's constant, $T$ is the gas temperature, and $m_{ij}$ is the reduced mass of the two particles.

The original design to connect the reactor to the DMA included 1.6 m of half inch line in between the two setups. For a deposition rate of 0.5 mg/min, this gives a distance of 0.759 mm before coagulation occurs. This is an underestimate because the image charge created by the few charged particles on the neutral particles will increase the capture radius for collisions that will lead to coagulation, which is not considered in equation 2.5. Moving the reactor tube closer to the DMA should improve this, but it will not completely remove the problem. There is a minimum path length due to the fact that the electrode column itself is 30 cm long. It was possible to reduce the length of the aerosol line from 1.6 m to 23 cm. The effect of shortening the path length is shown

figure 2.4. Unexpectedly, the longer path length appears to show a higher concentration of smaller particles than the shorter path length. This may be misleading because at least part of the distribution for both lengths is past the point that can be observed by the DMA. Also, the coagulation model described earlier does not account for loss of particles to the walls. It is possible that the concentration of particles is decreased enough to affect the size distribution by particles impacting the walls during the turns in the longer path.

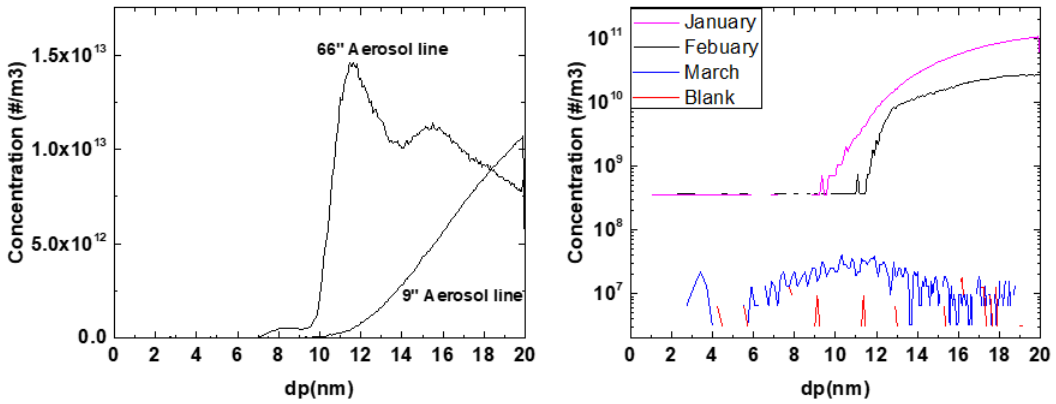


Figure 2.4: Effect of Shortening Aerosol Path Length
**Left:** Increase in particle concentration after shortening aerosol line. **Right:** Decrease in signal over time. Note that concentration is shown with a log scale.

Moving the reactor tube closer to the DMA did little to narrow the observed size distributions and caused a new problem to arise, the concentration of particles reaching the electrode and sensor was too high. The electronic equipment would become coated with silicon after several runs, causing the signal to gradually decrease over time. A solution to this is to decrease the amount of particles reaching the DMA from the plasma. This was achieved by inserting a mesh, so that the many of the particles would be caught by this mesh without increasing the pressure in the plasma. As shown in the left of figure 2.5, this greatly improved the signal coming from the DMA. It takes longer for the electrode to become coated, which increases possible run time before cleaning is necessary, and also seems to decrease the amount of coagulation experienced by the particles that reach the sensor stage.

However, the mesh takes some finite time to 'cake' with particles, and the signal

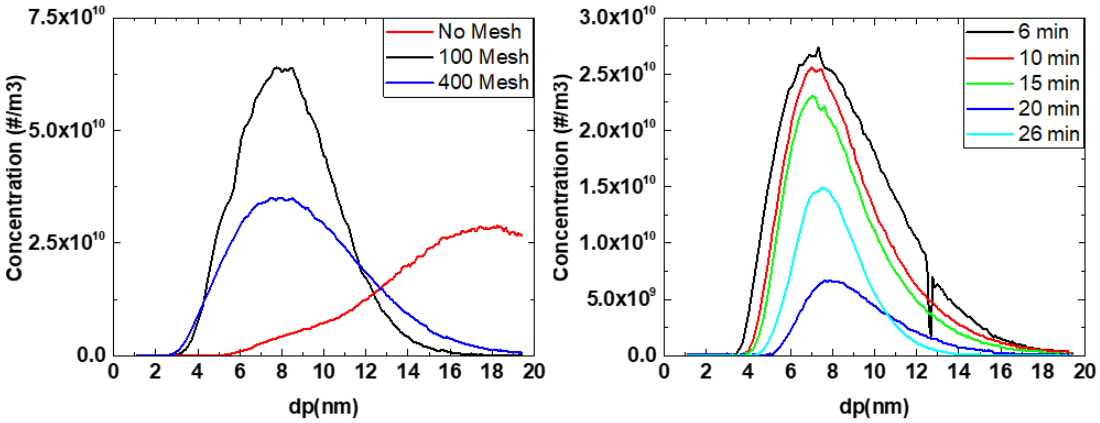


Figure 2.5: Effect of inserting a mesh near the outlet of the plasma reactor **Left:** Inserting a mesh significantly decreases the broadness of the distribution. **Right:** Signal change as the same mesh is used repeatedly. These are the results for a size 400 mesh.

will gradually decrease in magnitude until the mesh is full. Also, the pressure in the reactor tube is not being monitored, because the pressure gauge is downstream of the mesh. If the pressure increases significantly in the tube due to the mesh caking, it will change the size of produced particles. Tests using the same mesh repeatedly show that while the signal magnitude does decrease over time, the peak location does not shift, and the peak shape does not change for up to one hour using size 100 mesh. This can be taken as evidence that it is viable to take stable measurements using a mesh. The size distribution is still broad compared to that seen in TEM, but it is possible to see the expected linear relationship between residence time and particle size [18] as shown in figure 2.6.

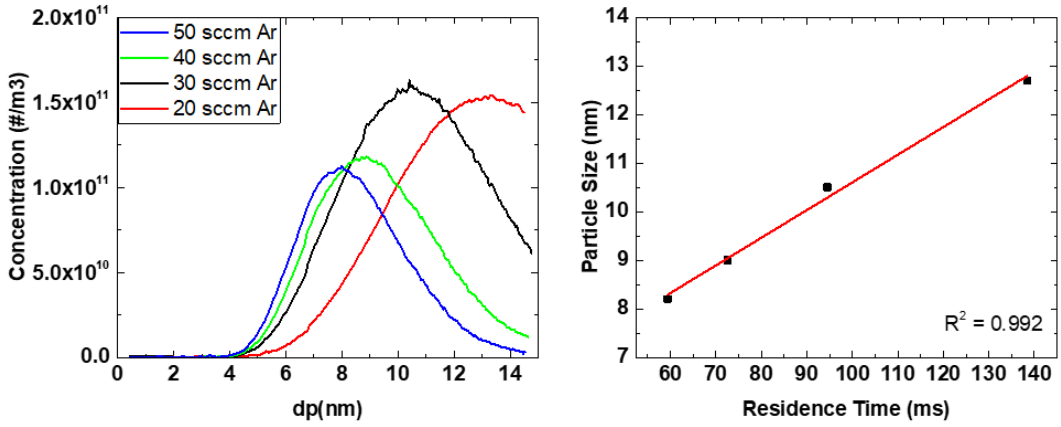


Figure 2.6: Argon Flow Study

**Left:** Size distributions change corresponding to argon flowrate. Silane and nitrogen flowrate were held at 6 sccm and 910 sccm respectively. Pressure was allowed to change with the changing argon flow. **Right:** Particle size as a function of residence time. The reported diameters are the peak locations found by fitting the curves shown in the left side of this figure as gaussian.

## 2.6 Interference

Moving the reactor tube closer to the DMA also caused an interference problem. The power supply for the DMA's electrode would not respond to commands when the plasma was on, and scans of an argon plasma only displayed a square wave, such as that shown in figure 2.7. This square wave reaches 6 V, while signal from the particles does not exceed 2 V.

Not only the plasma, but also the matchbox was found to be a major source of interference. Covering the reactor tube and the matchbox in copper mesh to serve as a Faraday shield allowed regained control of the DMA power supply. Increased grounding of the top and bottom of the reactor tube also decreased the noise observed in the electrometer.

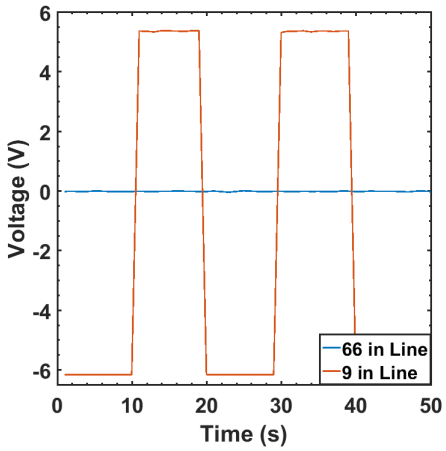


Figure 2.7: Interference Signal from the Plasma
DMA scan taken of an unshielded argon plasma.

## 2.7 Biased Mesh

In an effort to combat agglomeration, the mesh was given a bias. As discussed in section 2.4, neutralization of the particles that allows for agglomeration is believed to occur because the plasma's sheath acts as a natural neutralizer for the particles. Inserting a mesh raised to the potential of the plasma could prevent the formation of the sheath, allowing the particles to remain negatively charged, discouraging agglomeration. The original design for the biased mesh is show in figure 2.8.

The plastic mesh holder is inserted into the KF fitting downstream of the plasma outlet to prevent the mesh from contacting the surrounding metal. The negative end of the circuit is attached to stainless steel fittings that the plasma is in contact with so that the mesh is biased with respect to the plasma potential. Initial tests showed that biasing the mesh did not have any effects other than those observed with an unbiased mesh. A 100 Ω resistor was added between the plasma and the power supply in an attempt to observe the floating potential of the plasma, but no measurable current was found over the resistor.

The lack of change observed in response to biasing the mesh was attributed to the plasma not making contact with the mesh. Attempts were made to ensure contact by lowering the electrodes closer to the mesh. The electrodes are normally located at 3

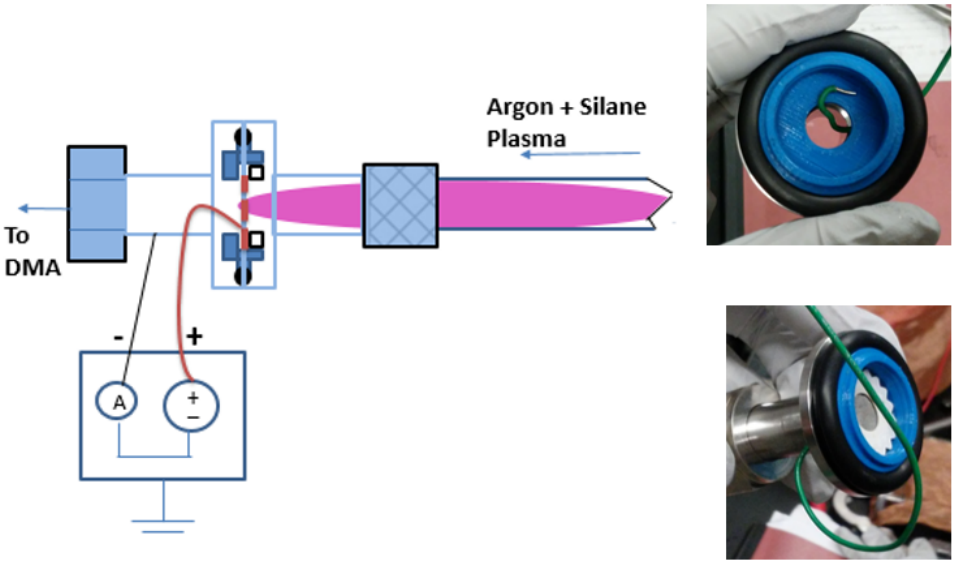


Figure 2.8: Schematic for the Biased Mesh
**Left:** Schematic of the placement of the biased mesh. A wire is allowed to contact the mesh which should be in contact with the plasma. The other end of the wire is attached to a DC power supply which provides the bias. **Upper Right:** The wire is wedged in between the bottom of the mesh holder and the mesh. **Lower Right:** Another plastic piece is inserted on top of the mesh. The wire is threaded through a hole in the stainless steel fitting downstream of the plasma.

and 5 cm from the bottom ultratorr that holds the reactor tube. With the grounded electrode 1 cm from the bottom ultratorr, particle growth was not observed. Results similar to those shown in figure 2.9 were observed with the electrodes at 2 and 4 cm. To remedy this, the mesh was bent into a bowl shape and inserted into the tube, where it be seen to make visible contact with the plasma. A RLC filter with a cut off frequency of 160 kHz was also added between the plasma and the DC power supply to protect the measuring equipment from the high frequency signal coming from the rf power supply that generates the plasma. Moving the mesh into the tube changes the structure of the plasma by preventing it from coupling to the bottom stainless steel fitting. The plasma is no longer able to generate particles in this state, and a lack of amorphous build up on the walls implies that the plasma conditions are so changed that it is no longer able to dissociate silane. The electrodes were moved upstream to allow the outlet of the plasma

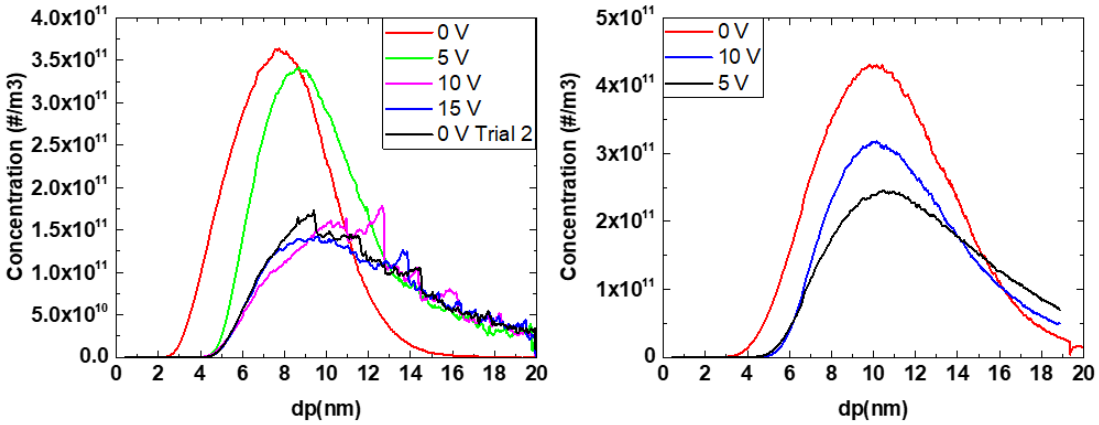


Figure 2.9: Scans Using Biased Mesh in Holder
**Left:** Scans taken with size 400 mesh. The change at 10 V is attributed to the mesh caking with particles rather than any effect of the bias, due to the fact the 0 V scan take afterwards has the same shape. **Right:** Scans taken with size 100 mesh. Broadening of the size distribution seems to correspond to length of time with the mesh in.

to make contact with the mesh, but also allow the plasma to couple to the top ultratorr fitting.

With the mesh in visible contact with the plasma, increasing the bias on the mesh causes the movement of striations along the bulk of the plasma. The distances between the ultratorr fitting, the electrodes and the mesh have great effect on the scans observed. Many configurations do not produce particles. Placing the mesh too close to the powered electrode causes the mesh to smolder, and metal deposition can be seen on the tube after etching away the silicon with KOH. It is possible to measure a current over the resistor in the RLC current when the plasma is on but the DC power supply is not. Because the measured current is in the $\mu$A range, it is difficult to measure repeatably with the tools available to the author. The 100 $\Omega$ resistor originally installed was replaced with a 2 $\Omega$ resistor in order to increase the magnitude of the current by decreasing the resistance, but the current was still too low to measure reliably with a multimeter. Results are summarized in figure 2.11

Particle scans show no clear trend in response to mesh bias, have lower signal than scans taken with the mesh in the ultratorr fitting, and are largely unrepeatable. The

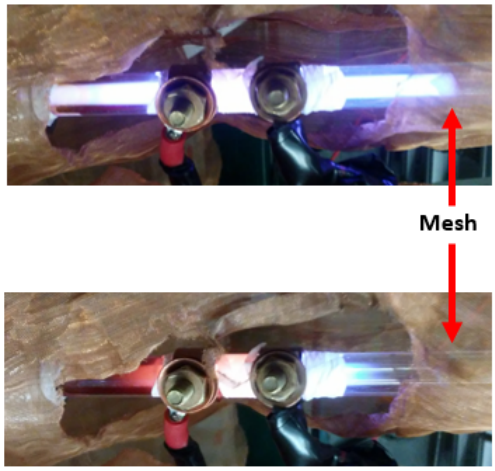


Figure 2.10: Loss of Contact with Plasma
**Top:** Immediately after striking an argon - silane plasma. **Bottom:** The same plasma after 15 minutes.

narrowest distributions were observed with the mesh very close to the powered electrode, but because the mesh begins to smolder after about 15 minutes, it is difficult to take many scans in this configuration. Another challenge of implementing the biased mesh is the build up of particles over time. At the beginning of deposition, the visible portion of the discharge appears to stop cleanly at the mesh surface. After several minutes of deposition however, the mesh becomes covered in silicon and the plasma no longer makes contact with the mesh.

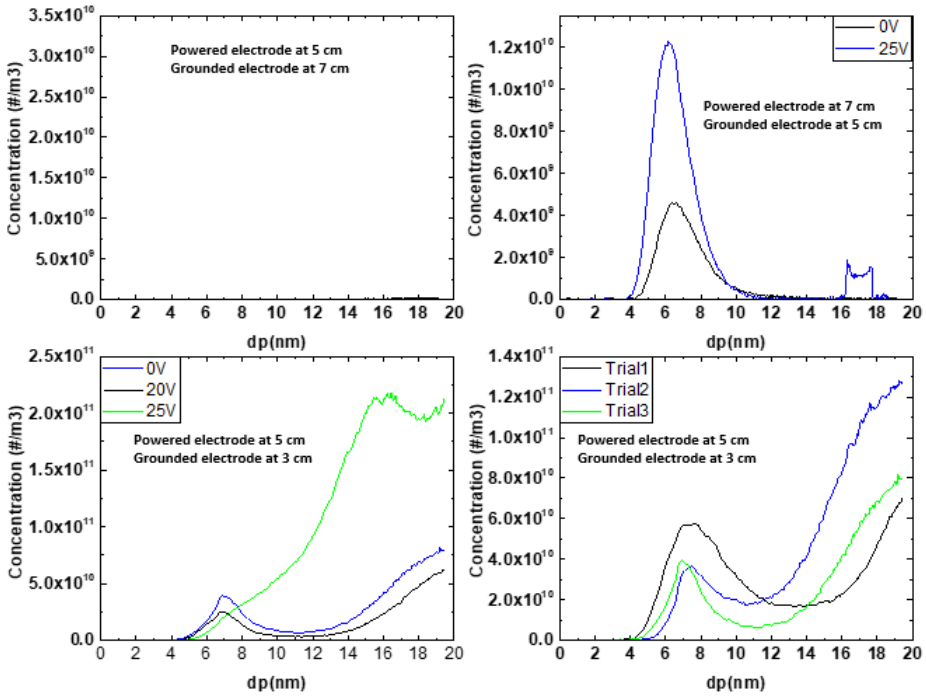


Figure 2.11: Scans Using Biased Mesh Inserted into Tube
**Top Left:** Powered electrode at 5 cm and grounded electrode at 7 cm from top ultratorr. No particle growth was observed, and abnormally little amorphous film growth was seen on tube. **Top Right:** Powered electrode at 7 cm and grounded electrode at 5 cm. In this configuration, the mesh glowed and metal deposition was observed on the tube. **Bottom Left:** Powered electrode at 5 cm and grounded electrode at 3 cm. This configuration corresponds to the images in figure 2.10. **Bottom Right:** Powered electrode at 5 cm and grounded electrode at 3 cm. Scans were taken with the same mesh over a period of 20 minutes.

## 2.8 Conclusion

Roughly equal numbers of positive and negative particles were measured in the plasma output, implying that the vast majority of the particles are neutrally charged. Only the charged particles can be selected by the DMA, so without modification the system cannot be used to collect monodisperse particles from the DMA output. The charge distribution also likely encourages in flight coagulation of the particles. Coagulation was found to be a major challenge for integrating the plasma and DMA system. The size distributions seen from the DMA are much broader and show a larger peak diameter

than what would be expected from TEM or XRD measurements. Inserting a mesh downstream of the plasma greatly improves the shape of the distribution by lowering the concentration of particles in flight, but does not completely remove the effects of coagulation. In spite of this, the expected relationship between size distribution and flowrate is still observable. Initial attempts were made to improve the action of the mesh by applying a bias, but a variety of challenges remain before the biased mesh is a useful tool.

## 2.9 Future Work

The most pressing future challenge of this work is how to reduce the broadening of the observed size distribution. Estimations show that coagulation is almost certainly occurring along the path length between the outlet of the plasma and the DMA's electrometer. It may be possible to further reduce the effects of coagulation by finding ways of decreasing the concentration of particles along the pathlength. Some of the broadening is also due to the effects of Brownian diffusion discussed in the introduction section. Altering the transfer function used to convert the signal from the DMA into a size distribution would likely be the most effective way of dealing with this type of broadening. If the transfer function is changed, many of the experiments recorded in this work will need to be reevaluated.

Once the distribution broadening is controlled, it should be possible to use the DMA to get data about how various process conditions affect the size distributions of the particles. The effects of changing flowrates, changing the pressure using an orifice, and reactor tube diameter and length can all be studied. The effects of hydrogen injection might be particularly interesting, considering hydrogen injection is considered crucial to improving quantum yield in gas phase nanoparticle synthesis. [36]

Further study of the effects of the biased mesh on size distribution may also be interesting. The largest challenge in continuing this work will likely be dealing the the fact that as silicon builds up on the mesh, the coupling of the plasma changes. It may be necessary to run the plasma for a certain length of time before taking measurements to ensure that the plasma will not change during the measurement. There is also the fact that biasing the mesh is clearly not only effecting the plasma sheath, but the entire

bulk of the plasma. This means that being very careful to always insert the mesh into the the exact same location will be very important to achieving repeatable results.

# References


[1] Catherine J. Murphy and Jeffery L. Coffer. Quantum Dots: A Primer. *Applied Spectroscopy*, 56(1):16–27, 2002.

[2] Justin D. Holmes, Kirk J. Ziegler, R. Christopher Doty, Lindsay E. Pell, Keith P. Johnston, and Brian A. Korgel. Highly luminescent silicon nanocrystals with discrete optical transitions. *Journal of the American Chemical Society*, 123(16):3743–3748, 2001.

[3] David Jurbergs, Elena Rogojina, Lorenzo Mangolini, and Uwe Kortshagen. Silicon nanocrystals with ensemble quantum yields exceeding 60%. *Applied Physics Letters*, 88(23):2004–2007, 2006.

[4] Alexandre M. P. Botas, Rebecca J. Anthony, Jeslin Wu, David J. Rowe, Nuno J. O. Silva, Uwe Kortshagen, Rui N. Pereira, and Rute A. S. Ferreira. Influence of the surface termination on the light emission of crystalline silicon nanoparticles. *Nanotechnology*, 27(32):325703, 2016.

[5] Rebecca Anthony and Uwe Kortshagen. Photoluminescence quantum yields of amorphous and crystalline silicon nanoparticles. *Physical Review B*, 80(11):115407, 2009.

[6] Uwe R. Kortshagen, R. Mohan Sankaran, Rui N. Pereira, Steven L. Girshick, Jeslin J. Wu, and Eray S. Aydil. Nonthermal Plasma Synthesis of Nanocrystals: Fundamental Principles, Materials, and Applications. *Chemical Reviews*, page acs.chemrev.6b00039, 2016.

[7] Huang Wei-Qi, Wang Hai-Xu, Jin Feng, and Qin Cao-Jian. Trap states in oxidation layer of nanocrystal Si. *Chinese Physics B*, 17(10), 2008.

[8] Steffen Hallmann, Mark J. Fink, and Brian S. Mitchell. Williamson ether synthesis: an efficient one-step route for surface modifications of silicon nanoparticles. *Journal of Experimental Nanoscience*, 10(8):588–598, 2015.

[9] Ants Tuulmets, Anu Ploom, Dmitri Panov, and Jaak Järv. Selectivity in the grignard reaction with silanes. *Synlett*, (2):291–293, 2010.

[10] Oleg Golubev, Dmitri Panov, Anu Ploom, Ants Tuulmets, and Binh T. Nguyen. Quantitative substituent effects in the Grignard reaction with silanes. *Journal of Organometallic Chemistry*, 692(17):3700–3705, 2007.

[11] Jillian M. Buriak. Organometallic Chemistry on Silicon and Germanium Surface. *Chem. Rev.*, 102(5):1271, 2002.

[12] Ashish Bansal, Xiuling Li, Iver Lauermann, and Nathan S Lewis. Alkylation of Si Surfaces Using a Two-Step Halogenation / Grignard Route. *Journal of the American Chemical Society*, 118(11):7225–7226, 1996.

[13] L. Mangolini, E. Thimsen, and Uwe Kortshagen. High-yield plasma synthesis of luminescent silicon nanocrystals. *Nano Letters*, 5(4):655–659, 2005.

[14] Riku Yamda, Ryan Gresback, Ding Yi, Ken Okazaki, and Tomohiro Nozaki. Plasma Synthesis of Silicon Nanoparticles: Optimization of Yield, Size Distribution, and Crystallinity. *Transactions of the Japan Society of Mechanical Engineers Series B*, 79(804):1616–1623, 2013.

[15] Ozgul Yasar-Inceoglu, Thomas Lopez, Ebrahim Farshihagro, and Lorenzo Mangolini. Silicon nanocrystal production through non-thermal plasma synthesis: a comparative study between silicon tetrachloride and silane precursors. *Nanotechnology*, 23(25):255604, 2012.

[16] Lance M. Wheeler. *Surface Engineering of Colloidal Group IV Nanocrystals for Optoelectronics*. Doctoral thesis, University of Minnesota, 2014.

[17] Michael A. Lieberman and Allan J. Lichtenberg. *Principles of Plasma Discharges and Materials Processing*. Wiley, Hoboken, second edition, 2005.

[18] Ryan Gresback, Zachary Holman, and Uwe Kortshagen. Nonthermal plasma synthesis of size-controlled, monodisperse, freestanding germanium nanocrystals. *Applied Physics Letters*, 91(9):9–11, 2007.

[19] Ryan Gresback, Tomohiro Nozaki, and Ken Okazaki. Synthesis and oxidation of luminescent silicon nanocrystals from silicon tetrachloride by very high frequency nonthermal plasma. *Nanotechnology*, 22(30):305605, 2011.

[20] Tomohiro Nozaki, Kenji Sasaki, Tomohisa Ogino, Daisuke Asahi, and Ken Okazaki. Microplasma synthesis of tunable photoluminescent silicon nanocrystals. *Nanotechnology*, 18:235603, 2007.

[21] Yeshi Ma, Xiaobo Chen, Xiaodong Pi, and Deren Yang. Theoretical study of chlorine for silicon nanocrystals. *Journal of Physical Chemistry C*, 115(26):12822–12825, 2011.

[22] A. N. Poddubny and K. Dohnalová. Direct band gap silicon quantum dots achieved via electronegative capping. *Physical Review B - Condensed Matter and Materials Physics*, 90(24):1–7, 2014, arXiv:1405.6259v1.

[23] Mita Dasog, Kathrin Bader, and Jonathan G C Veinot. Influence of halides on the optical properties of silicon quantum dots. *Chemistry of Materials*, 27(4):1153–1156, 2015.

[24] Lance M. Wheeler, Laszlo M. Levij, and Uwe R. Kortshagen. Tunable band gap emission and surface passivation of germanium nanocrystals synthesized in the gas phase. *Journal of Physical Chemistry Letters*, 4(20):3392–3396, 2013.

[25] Zachary C. Holman, Chin Yi Liu, and Uwe R. Kortshagen. Germanium and silicon nanocrystal thin-film field-effect transistors from solution. *Nano Letters*, 10(7):2661–2666, 2010.

[26] Joseph B. Miller, Austin R. Van Sickle, Rebecca J. Anthony, Daniel M. Kroll, Uwe R. Kortshagen, and Erik K. Hobbie. Ensemble brightening and enhanced

quantum yield in size-purified silicon nanocrystals. *ACS Nano*, 6(8):7389–7396, 2012.

[27] C. Xu, Z. P. Li, W. Pan, and W. Z. Shen. Tuning photoresponse through size distribution control of silicon quantum dots. *Applied Surface Science*, 257(20):8409–8412, 2011.

[28] Amanda M Nienow and Jeffrey T Roberts. Chemical Vapor Deposition of Zirconium Oxide on Aerosolized Silicon Nanoparticles. *Chemistry of Materials*, (8):5571–5577, 2006.

[29] Kwang Soo Seol, Yasuyuki Tsutatani, Toshiyuki Fujimoto, Yoshiki Okada, Kazuo Takeuchi, and Hidetoshi Nagamoto. New in situ measurement method for nanoparticles formed in a radio frequency plasma-enhanced chemical vapor deposition reactor. *Journal of Vacuum Science & Technology B: Microelectronics and Nanometer Structures*, 19:1998, 2001.

[30] Manuel Alonso, Francisco José Alguacil, and Virginia Gómez. Approximate relationship between voltage and mobility for Brownian particles in cylindrical DMAs. *Journal of Aerosol Science*, 58:62–70, 2013.

[31] E. O. Knutson and K. T. Whitby. Aerosol classification by electric mobility: apparatus, theory, and applications. *Journal of Aerosol Science*, 6(6):443–451, 1975.

[32] Y. Kousaka, K. Okuyama, and M. Adachi. Determination of Particle Size Distribution of Ultra-Fine Aerosols Using a Differential Mobility Analyzer. *Aerosol Science and Technology*, 4(2):209–225, 1985.

[33] Chunshi Cui and J. Goree. Fluctuations of the Charge on a Dust Grain in a Plasma. *IEEE Transactions on Plasma Science*, 22(2):151–158, 1994, arXiv:1011.1669v3.

[34] Themis Matsoukas and Marc Russell. Particle charging in low-pressure plasmas. *Journal of Applied Physics*, 77(9):4285–4292, 1995.

[35] Pulkit Agarwal and Steven L Girshick. Sectional modeling of nanoparticle size and charge distributions in dusty plasmas. *Plasma Sources Science and Technology*, 21(5):055023, 2012.

[36] Rebecca J. Anthony, David J. Rowe, Matthias Stein, Jihua Yang, and Uwe Kortshagen. Routes to achieving high quantum yield luminescence from gas-phase-produced silicon nanocrystals. *Advanced Functional Materials*, 21(21):4042–4046, 2011.